

Towards human SuperEEG

Lucy L. W. Owen¹, Andrew C. Heusser^{1,2}, and Jeremy R. Manning^{1*}

¹Department of Psychological and Brain Sciences, Dartmouth College,
Hanover, NH 03755, USA
²Akili Interactive,
Boston, MA 02110, USA

Abstract

Human *SuperEEG*¹ entails measuring ongoing neural activity with perfect precision and at arbitrarily high spatiotemporal resolution. Although true SuperEEG is impossible using existing methods, here we present a model-based method for *inferring* neural activity at millimeter-scale spatial resolutions and millisecond-scale temporal resolutions using standard human intracranial recordings. Our approach assumes that different people’s brains exhibit similar spatial correlations, and that (all else being equal) neural activity at nearby locations will tend to be similar. One can then ask, for an arbitrary individual’s brain: given recordings from a limited set of locations in that individual’s brain, along with the observed spatial correlations in other people’s recordings, what would recordings most likely have looked like at *other* locations in that individual’s brain?

Introduction

Modern human brain recording techniques are fraught with compromise [2]. Commonly used approaches include functional magnetic resonance imaging (fMRI), scalp electroencephalography (EEG), and magnetoencephalography (MEG). For each of these techniques, neuroscientists and electrophysiologists must choose to optimize spatial resolution at the cost of temporal resolution (e.g. as in fMRI) or temporal resolution at the cost of spatial resolution (e.g. as in EEG and MEG). A less widely used approach (due to requiring work with neurosurgical patients) is to record from electrodes implanted directly onto the cortical surface (electrocorticography; ECoG) or into deep brain structures (intracranial EEG; iEEG). However, these intracranial approaches also require compromise: the high temporal and spatial resolutions of intracranial recordings comes at the cost of substantially reduced brain coverage, since safety

¹The term “SuperEEG” was coined by Robert J. Sawyer in his popular science fiction novel *The Terminal Experiment* [1].

23 considerations limit the number of electrodes one may implant in a given patient's brain. Further, the
24 locations of implanted electrodes are determined by clinical, rather than research, needs.

25 An increasingly popular approach is to improve the effective spatial resolution of MEG or scalp
26 EEG data by using a geometric approach called *beamforming* to solve the biomagnetic or bioelectrical
27 inverse problem [3]. This approach entails using detailed brain conductance models (often informed
28 by high spatial resolution anatomical MRI images) along with the known sensor placements (localized
29 precisely in 3D space) to reconstruct brain signals originating from theoretical point sources deep in the
30 brain (and far from the sensors). Traditional beamforming approaches must overcome two obstacles.

31 First, the inverse problem beamforming seeks to solve has infinitely many solutions. Researchers have
32 made traction towards constraining the solution space by assuming that signal-generating sources are
33 localized on a regularly spaced grid spanning the brain and that individual sources are small relative to
34 their distances to the sensors [4–6]. The second, and in some ways much more serious, obstacle is that
35 the magnetic fields produced by external (noise) sources are substantially stronger than those produced
36 by the neuronal changes being sought (i.e. at deep structures, as measured by sensors at the scalp). This
37 means that obtaining adequate signal quality often requires averaging the measured responses over tens
38 to hundreds of responses or trials (e.g. see review by [6]).

39 Another approach to obtaining high spatial and temporal resolution neural data has been to collect
40 fMRI and EEG data simultaneously. Simultaneous fMRI-EEG has the potential to balance the high spa-
41 tial resolution of fMRI with the high temporal resolution of scalp EEG, thereby, in theory, providing the
42 best of both worlds. In practice, however, the signal quality of both recordings suffers substantially when
43 the two techniques are applied simultaneously (e.g. see review by [7]). In addition, the experimental
44 designs that are ideally suited to each technique individually are somewhat at odds. For example, fMRI
45 experiments typically lock stimulus presentation events to the regularly spaced image acquisition time
46 (TR), which maximizes the number of post-stimulus samples. By contrast, EEG experiments typically
47 employ jittered stimulus presentation times to maximize the experimentalist's ability to distinguish elec-

48 trical brain activity from external noise sources such as from 60 Hz alternating current power sources.
49 The current “gold standard” for precisely localizing signals and sampling at high temporal resolution
50 is to take (ECoG or iEEG) recordings from implanted electrodes (but from a limited set of locations in
51 any given brain). This begs the following question: what can we infer about the activity exhibited by
52 the rest of a person’s brain, given what we learn from the limited intracranial recordings we have from
53 their brain and additional recordings taken from *other* people’s brains? Here we develop an approach,
54 which we call *SuperEEG*, based on Gaussian process regression [8]. SuperEEG entails using data from
55 multiple people to estimate activity patterns at arbitrary locations in each person’s brain (i.e., independent
56 of their electrode placements). We test SuperEEG approach using two large datasets of intracranial
57 recordings [9–22]. We show that the SuperEEG algorithm recovers signals well from electrodes that were
58 held out of the training dataset. We also examine the factors that influence how accurately activity may
59 be estimated (recovered), which may have important implications for electrode design and placement in
60 neurosurgical applications.

61 Approach

62 The SuperEEG approach to inferring high temporal resolution full-brain activity patterns is outlined and
63 summarized in Figure 1. We describe (in this section) and evaluate (in *Results*) our approach using a two
64 large previously collected dataset comprising multi-session intracranial recordings. Dataset 1 comprises
65 multi-session recordings taken from 6876 electrodes implanted in the brains of 88 epilepsy patients [9–
66 13]. Each recording session lasted from XXX–XXX hours, and includes data recorded roughly from
67 when the patients woke up each morning, to before they went to sleep at the end of each day. In addition
68 to typical bed-ridden hospital patient activities (e.g., lying in bed, reading, watching television, using
69 personal electronic devices, listening to music, visiting with family and friends, etc.), the patients also
70 performed a variety of experimental cognitive tasks throughout their day (primarily list-learning memory
71 tasks). For the purposes of the Dataset 1 analyses presented here, we aggregated all data across each

72 recording session, ignoring the particular activities or tasks the patients were performing at any given
73 moment. We used Dataset 1 to develop and debug our main SuperEEG approach, and to examine the
74 extent to which SuperEEG might be able to generate task-general predictions. Dataset 2 comprised
75 multi-session recordings from XXX electrodes implanted in the brains of XXX epilepsy patients [14–
76 22]. Whereas Dataset 1 included recordings taken during a wide variety of behaviors, Dataset 2 included
77 recordings taken as each patient performed each of two memory tasks: a random word list free recall
78 task and a categorized word list free recall task. We used Dataset 2 to further examine the ability of
79 SuperEEG to generalize its predictions within versus across tasks.

80 **JRM STOPPED HERE**

81 The first dataset was taken from 6876 electrodes implanted in the brains of 88 epilepsy patients [9–
82 13]. We first applied a fourth order Butterworth notch filter to remove 60 Hz ($\pm .5$ Hz) line noise. We
83 then excluded any electrodes that showed putative epileptiform activity. Specifically, we excluded from
84 further analysis any electrode that exhibited an average kurtosis of 10 or greater across all of that patient’s
85 recording sessions. We also excluded any patients with fewer than 2 electrodes that passed this criteria,
86 as the SuperEEG algorithm requires measuring correlations between 2 or more electrodes from each
87 patient. Altogether this yielded clean recordings from 4168 electrodes implanted throughout the brains
88 of 67 patients (Fig. 1A). For the purposes of comparing task-specific contributions to reconstruction
89 accuracy, we limited our analyses in the second dataset to patients that participated in two free recall
90 experiments. Applying the same kurtosis thresholding yielded clean recordings from 24 patients and
91 2975 electrodes for the second dataset. Each individual patient contributes electrodes from a limited set
92 of brain locations, which we localized in a common space (MNI152); an example patient’s 54 electrodes
93 that passed the predefined kurtosis test are highlighted in black and red.

94 The recording from a given electrode is maximally informative about the activity of the neural tissue
95 immediately surrounding its recording surface. However, brain regions that are distant from the record-
96 ing surface of the electrode also contribute to the recording, albeit (often) to a much lesser extent. One

97 mechanism underlying these contributions is volume conduction. The precise rate of falloff due to vol-
 98 ume conduction (i.e. how much a small volume of brain tissue at location x contributes to the recording
 99 from an electrode at location η) depends on the size of the recording surface, the electrode's impedance,
 100 and the conductance profile of the volume of brain between x and η . As an approximation of this in-
 101 tuiton, we place a Gaussian radial basis function (RBF) at the location η of each electrode's recording
 102 surface (Fig. 1B). We use the values of the RBF at any brain location x as a rough estimate of how much
 103 structures around x contributed to the recording from location η :

$$\text{rbf}(x|\eta, \lambda) = \exp \left\{ -\frac{\|x - \eta\|^2}{\lambda} \right\}, \quad (1)$$

104 where the width variable λ is a parameter of the algorithm (which may in principle be set according to
 105 location-specific tissue conductance profiles) that governs the level of spatial smoothing. In choosing λ
 106 for the analyses presented here, we sought to maximize spatial resolution (which implies a small value
 107 of λ) while also maximizing the algorithm's ability to generalize to any location throughout the brain,
 108 including those without dense electrode coverage (which implies a large value of λ). Using our prior
 109 work as a guide [23], we set $\lambda = 20$, although this could in theory be optimized, e.g. using cross
 110 validation.

111 A second mechanism whereby a given region x can contribute to the recording at η is through
 112 anatomical connections between structures near x and η . We use spatial correlations in the data to
 113 estimate these anatomical connections. Let \bar{R} be the set of locations at which we wish to estimate local
 114 field potentials, and let R_s be set of locations at which we observe local field potentials from patient
 115 s (excluding the electrodes that did not pass the kurtosis test described above). In the analyses below
 116 we define $\bar{R} = \cup_{s=1}^S R_s$. We can calculate the expected inter-electrode correlation matrix for patient s ,
 117 where $C_{s,k}(i, j)$ is the correlation between the time series of voltages for electrodes i and j from subject
 118 s during session k , using:

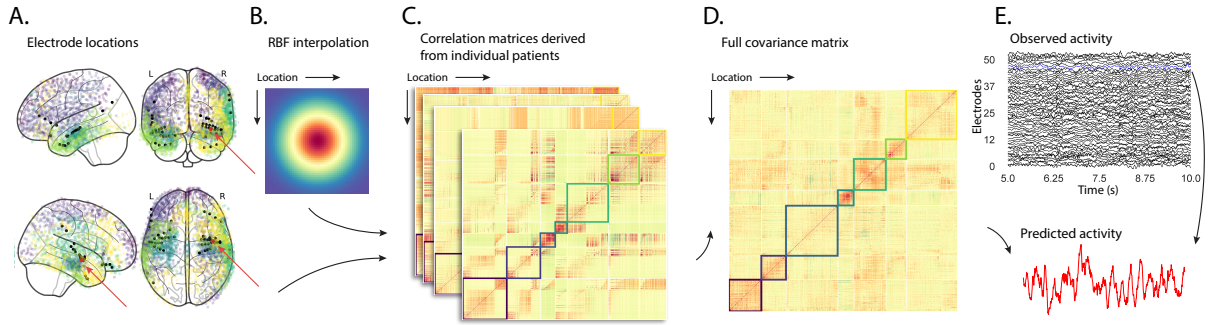


Figure 1: Methods overview. **A. Electrode locations.** Each dot reflects the location of a single electrode in dataset 1, colored according to 7 factor labels (see Panel D for details). One patient’s electrode locations are highlighted in black and the to-be-reconstructed recording location is highlighted in red. **B. Radial basis function (RBF).** Each electrode contributed by the patient (black) weights on the full set of locations under consideration (all dots in Panel A, defined as \bar{R} in the text). The weights fall off with positional distance (in MNI space) according to an RBF. **C. Per-patient correlation matrices.** After computing the pairwise correlations between the recordings from each patient’s electrodes, we use RBF-weighted averages to estimate correlations between all locations in \bar{R} . We obtain an estimated full-brain correlation matrix using each patient’s data. **D. Combined correlation matrix.** We estimate a single full-brain correlation matrix by averaging the patient-specific correlation matrices. We sort the resulting correlation matrix based on 7 factor labels obtained from k-means clustering [24]). **E. Reconstructing activity throughout the brain.** Given the observed activity from the patient’s electrodes and the estimated correlation matrix (Panel D), we can compute a maximum likelihood estimate of the voltage trace at any location in \bar{R} . An example reconstruction (at the red dot in Panel A) is shown in red, and the actual recording at that location is highlighted above in blue.

$$\bar{C}_s = r\left(\frac{1}{n}\left(\sum_{k=1}^n z(C_{s,k})\right)\right), \text{ where} \quad (2)$$

$z(r) = \frac{\log(1+r) - \log(1-r)}{2}$ is the Fisher z -transformation and (3)

$$z^{-1}(z) = r(z) = \frac{\exp(2z) - 1}{\exp(2z) + 1} \text{ is its inverse.} \quad (4)$$

119 Next, we use Equation 1 to construct a number of to-be-estimated locations by number of patient elec-
 120 trode locations weight matrix, W . Specifically, W approximates how informative the recordings at each
 121 location in R_s are in reconstructing activity at each location in \bar{R} , where the contributions fall off with
 122 an RBF according to the distances between the corresponding locations:

$$W(i, j) = \text{rbf}(i|j, \lambda). \quad (5)$$

123 Given this weight matrix, W , and the observed inter-electrode correlation matrix for patient s , \bar{C}_s ,
 124 we can estimate the correlation matrix for all locations in \bar{R} (Fig. 1C) using:

$$\hat{N}_s(x, y) = \sum_{i=1}^{|R_s|} \sum_{j=1}^{i-1} W(x, i) \cdot W(y, j) \cdot z(\bar{C}_s(i, j)) \quad (6)$$

$$\hat{D}_s(x, y) = \sum_{i=1}^{|R_s|} \sum_{j=1}^{i-1} W(x, i) \cdot W(y, j). \quad (7)$$

125 Intuitively, we construct an estimated correlation matrix from each individual patient's data (Fig. 1C)
 126 using Equations 6 & 7, then we sum across these estimates for S patients and divide (see Equations 8) to
 127 obtain the expected correlation matrix, \hat{K} (Fig. 1D):

$$\hat{K} = r \left(\frac{\sum \hat{N}_s}{\sum \hat{D}_s} \right). \quad (8)$$

¹²⁸ Now we can use the following intuition: given (i) the observed responses from a limited set of locations
¹²⁹ in R_s (Y_s) and (ii) how each location's responses relate to all other responses (\hat{K}), we can estimate the
¹³⁰ LFP data from patient s , for any arbitrary location in \bar{R} (Fig. 1E).

¹³¹ Let α be the set of indices of patient s 's electrode locations in \bar{R} , and let β be the set of indices of all
¹³² other locations in \bar{R} . In other words, β reflects the locations in \bar{R} where we did not observe a recording
¹³³ for patient s (these are the recording locations we will want to fill in using SuperEEG). We can sub-divide
¹³⁴ \hat{K} as follows:

$$\hat{K}_{\beta,\alpha} = \hat{K}(\beta, \alpha), \text{ and} \quad (9)$$

$$\hat{K}_{\alpha,\alpha} = \hat{K}(\alpha, \alpha). \quad (10)$$

¹³⁵ Here $\hat{K}_{\beta,\alpha}$ stores the correlations between the “unknown” activity at the locations in β and the observed
¹³⁶ activity at the locations in α , and $\hat{K}_{\alpha,\alpha}$ stores the correlations between the observed recordings (at the
¹³⁷ locations in α).

¹³⁸ Let $Y_{s,k,\alpha}$ be the number-of-timepoints (T) by $\text{length}(\alpha)$ matrix of (observed) voltages from the
¹³⁹ electrodes in α during session k from patient s . Then we can estimate the voltage from patient s 's k^{th}
¹⁴⁰ session at the locations in β using [8]:

$$Y_{s,k,\beta} = ((\hat{K}_{\beta,\alpha} \cdot \hat{K}_{\alpha,\alpha}^{-1}) \cdot Y_{s,k,\alpha}^T)^T. \quad (11)$$

¹⁴¹ This equation is the foundation of the SuperEEG algorithm. Whereas we observe the recordings only
¹⁴² at the locations in α , Equation 11 allows us to estimate the recordings at all locations in β , which we
¹⁴³ can define *a priori* to include any locations we wish, throughout the brain. This yields estimates of the
¹⁴⁴ time-varying voltages at *every* location in \bar{R} .

¹⁴⁵ We designed our approach to be agnostic to electrode impedances, as electrodes that do not exist do
¹⁴⁶ not have impedances. Therefore our algorithm recovers voltages in standard deviation (z -scored) units

rather than attempting to recover absolute voltages. (This property reflects the fact that $\hat{K}_{\beta,\alpha}$ and $\hat{K}_{\alpha,\alpha}$ are correlation matrices rather than covariance matrices.) Also, note that Equation 11 requires computing a T by T matrix, which can become computationally intractable when T is very large (e.g. for the patient highlighted in Fig. 2, $T = 20458799$). However, we may approximate $Y_{s,k,\beta}$ in a piecewise manner by filling in $Y_{s,k,\beta}$ in blocks of size b samples (using the corresponding samples from $Y_{s,k,\alpha}$). In our computations we set $b = 25000$.

The SuperEEG algorithm described above and in Figure 1 allows us to estimate (up to a constant scaling factor) LFPs for each patient at all arbitrarily chosen locations in the set \bar{R} , *even if we did not record that patient’s brain at all of those locations.*

Results

To test the accuracy with which the SuperEEG algorithm reconstructs activity throughout the brain, we held out each electrode from the full dataset in turn and treated it as unobserved. We then asked: how closely did each of the SuperEEG-reconstructed LFPs match the observed data? We sought to evaluate both the overall reconstruction accuracy as well as how reconstruction accuracy varied as a function of implantation location.

We first examined raw LFP traces and their associated Super EEG-derived reconstructions. Figure 2A displays the LFP from the red electrode in Figure 1A, and its associated reconstruction, during a 5 s time window during one of the patient’s 6 recording sessions. Figure 2B displays a 2D histogram of the observed versus reconstructed voltages for every sample across 14.2 total hours of recordings from that patient (correlation: $r = 0.91, p < 10^{-10}$). Although the SuperEEG algorithm recovered the recordings from this electrode well, we sought to quantify the algorithm’s performance across the full dataset.

Holding out each electrode from each patient in turn, we computed the average correlation (across recording sessions) between the Super EEG-reconstructed voltage traces and the observed voltage traces from that electrode. For each reconstruction, we estimated the full-brain correlation matrix using every

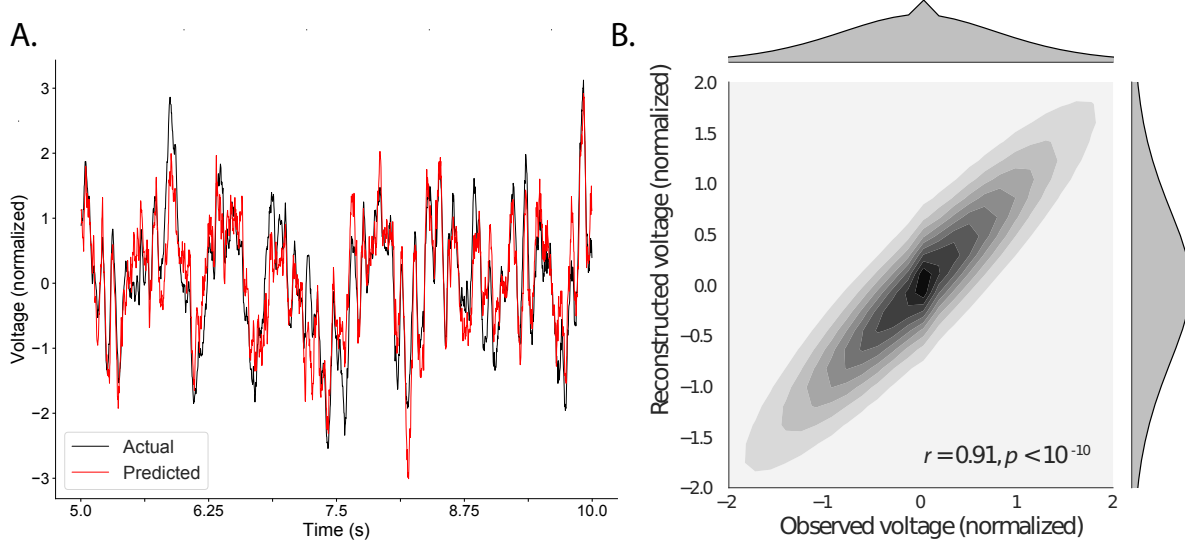


Figure 2: Observed and reconstructed LFP from a single electrode. A. Example LFP. A 2 s recording from the blue electrode in Figure 1A is displayed in red, and the reconstructed LFP during the same time window is shown in black. All voltages are plotted in standard deviation units. **B. Observed versus reconstructed voltages over 14.2 hours.** The 2D histogram reflects the relation between distributions of observed versus reconstructed voltages from one patient, across the 14.2 hours of recorded data collected in 6 recording sessions. The correlation reported in the panel is between the observed and reconstructed voltages.

¹⁷¹ *other* patient's data (i.e. every patient except the one who contributed the to-be-reconstructed electrode
¹⁷² data). In our analyses, we then substituted the average correlation matrix computed after excluding
¹⁷³ patient s 's data for \hat{K} in Equations 9 and 10. This step ensured that the data we were reconstructing
¹⁷⁴ could not also be used to estimate the between-location correlations that drove the reconstructions via
¹⁷⁵ Equation 11 (otherwise the analysis would be circular).

¹⁷⁶ We obtained a single correlation coefficient for each electrode location in \bar{R} , reflecting how well
¹⁷⁷ the SuperEEG algorithm was able to recover the recording at that location by incorporating data across
¹⁷⁸ patients (Across shown in black, see Fig. 3A). We also reconstructed activity for each electrode using a
¹⁷⁹ model trained on the remaining electrodes from only that patient, to account for reconstruction accuracy
¹⁸⁰ attributed to volume conductance alone (Within shown in gray, see Fig. 3A). For the first dataset, we
¹⁸¹ compared these two distributions of correlation coefficients (paired t -test between z -transformed mean
¹⁸² correlation coefficients by patient: $t(66) = 9.64, p < 10^{-10}$). We repeated this analysis on a similar
¹⁸³ dataset (Fig. 3C) with similar results (paired t -test between z -transformed mean correlation coefficients
¹⁸⁴ by patient: $t(23) = 6.93, p < 10^{-5}$). This is an especially conservative test, given that the SuperEEG
¹⁸⁵ reconstructions exclude (from the correlation matrix estimates) all data from the patient whose data is
¹⁸⁶ being reconstructed. Furthermore, we also replicated this finding for each independent experiment within
¹⁸⁷ dataset 2 (Fig. S3 (paired t -test between z -transformed mean correlation coefficients by patient for exper-
¹⁸⁸ iment 1: $t(23) = 6.23, p < 10^{-5}$ and experiment 2: $t(23) = 6.62, p < 10^{-5}$). That the SuperEEG-derived
¹⁸⁹ correlations were reliably stronger than these correlations obtained using a volume conductance null
¹⁹⁰ model is exciting for two reasons. First, it implies that distant electrodes provide additional predictive
¹⁹¹ power to the data reconstructions beyond the information contained in nearby electrodes. Second, it
¹⁹² implies that the spatial correlations driving the SuperEEG algorithm are, to some extent, shared across
¹⁹³ people.

¹⁹⁴ We were interested in the task specific contributions to the reconstruction accuracy. Each patient
¹⁹⁵ in the second dataset participated in two free recall experiments. We ran similar analyses for both

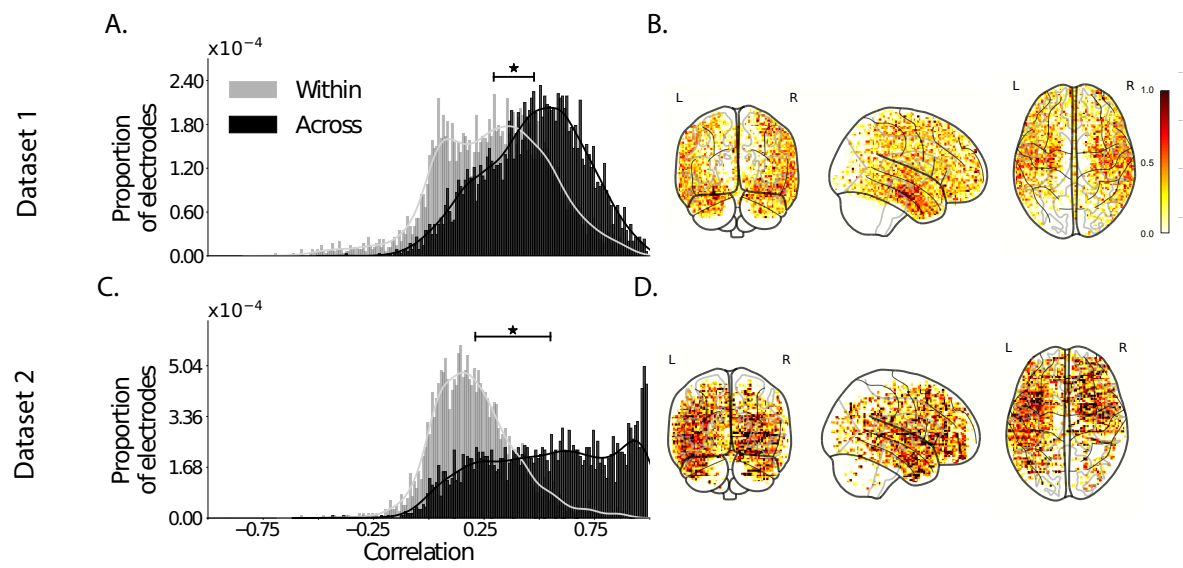


Figure 3: Reconstruction quality. A. & C. Distributions of correlation coefficients. Across all electrodes from all patients in the labeled dataset, the panel displays the distribution of correlations between the observed and reconstructed LFP data using models trained on data from all other patients (Across, in black) and all other electrodes from the same patient (Within, in gray). **B. & D. Correlation maps.** The glass brain maps display the average correlation between the observed LFP data and the across-subjects model reconstructed data by location, for each labeled experiment.

196 experiments and found that activity was best reconstructed when limiting the training data to within
197 task, as opposed to across task or incorporating data from both tasks (Fig. S1 (mean reconstruction
198 accuracy incorporating data within task: 0.55, across task: 0.37, all tasks: .50)). Although reconstruction
199 accuracy in the across task analysis was still better than the volume conductance model alone (paired
200 *t*-test between *z*-transformed mean correlation coefficients by patient: $t(47) = 5.65, p < 10^{-5}$), these
201 results suggests that having a common tasks for patients may yield better reconstruction accuracy.

202 We also wondered whether reconstruction quality (measured as the correlation between the observed
203 and reconstructed data) varied with the electrode locations (Fig. 3B & D). In general, reconstruction
204 quality remained high throughout the brain. Although reconstruction accuracy appeared high in the me-
205 dial temporal lobe, which is a common epileptic focus (and therefore a common target for electrode
206 implantation), we observed a weak but statistically reliable negative correlation between reconstruction
207 quality and electrode density (defined as the proportion of electrodes within 20 MNI units for each loca-
208 tion; dataset 1: $r = -0.07, p < 10^{-5}$, dataset 2: $r = -0.16, p < 10^{-10}$). This provides some evidence
209 that our reconstruction accuracy results cannot be driven only by volume conductance. Qualitatively, it
210 appeared that the distribution of electrodes was similar across the datasets, suggesting potential com-
211 monalities of target locations across patients and similarities in surgical decisions. Indeed, we found
212 a relatively strong correlation between the electrode densities within the two datasets (defined as the
213 proportion of electrodes within 20 MNI units for each 34686 voxels (Fig. 4A, B); $r = 0.57, p < 10^{-10}$).

214 In addition to exploring how reconstruction quality varies with location, we also wondered whether
215 there might be effects of electrode placements on reconstruction quality. For example, are there particular
216 implantation locations that yield especially high reconstruction accuracies at other locations throughout
217 the brain? To gain insights into this questions, we computed the average reconstruction correlation
218 for each patient, then computed the average patient reconstruction correlation for any patients who had
219 electrodes within a 20 MNI unit diameter sphere centered on each voxel location. The resulting maps
220 highlight the locations of implanted electrodes from patients whose reconstructions were especially ac-

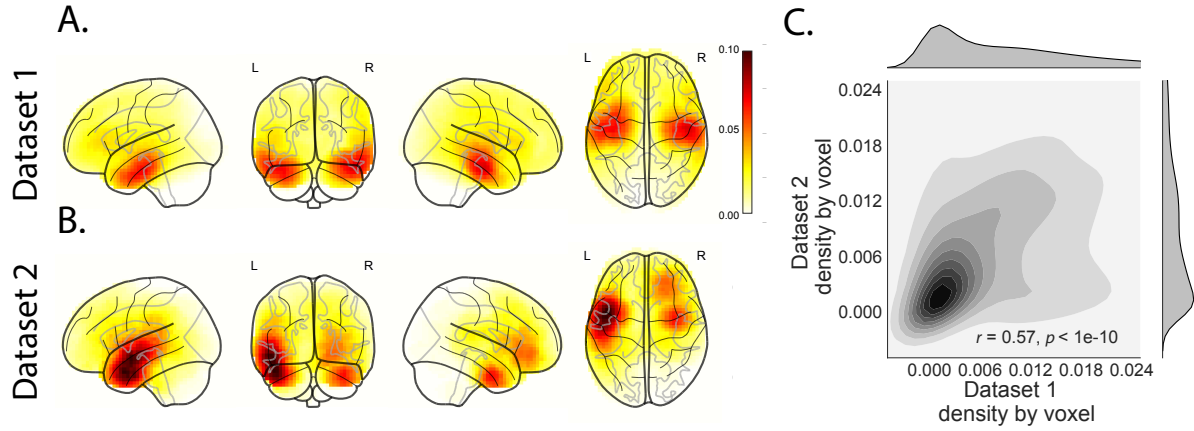


Figure 4: Sampling density and reconstruction quality. **A. & B.** The glass brain maps show sampling density by voxel location for dataset 1 and dataset 2. **C.** Correlation of sampling density by voxel location for dataset 1 vs. dataset 2.

221 curate (Fig. 5A and B). We found that the most informative locations were consistent across datasets
 222 which lends support to the notion that different electrode location are more informative about activity
 223 across patients (Fig. 5C); $r = 0.22, p < 10^{-10}$). The locations in dark red might therefore be good can-
 224 didate implantation targets for neurosurgeons and neurologists who wish to use SuperEEG to reconstruct
 225 full-brain electrophysiological signals. The above findings, that one can infer brain activity throughout a
 226 person's brain using recordings from a limited number of locations from that person's brain in conjunc-
 227 tion with recordings from other people's brains, have deep implications for the structure of brain data.
 228 The first implication is that the correlational structure of different people's brain data is largely preserved
 229 across individuals. Despite recent evidence that different people have stable but reliably different resting
 230 state connectome [25], our results suggest that the correlational structure of different people's brain data
 231 is preserved enough across individuals to provide meaningful information.

232 Discussion

233 SuperEEG infers full-brain activity patterns by leveraging correlations in those patterns of brain activity
 234 within and across people. Although the approach may, in principle, be used to infer brain activity *any-*

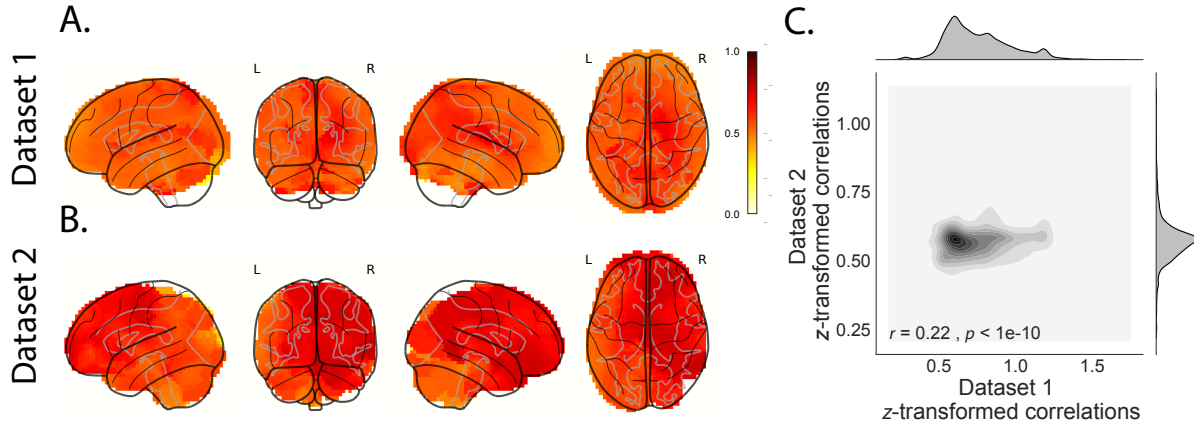


Figure 5: **Most informative electrode locations.** **A. & B.** The glass brain maps displays the average reconstruction correlations (by patient, across all electrodes) for patients with electrodes within a 20 MNI unit diameter sphere centered on each location for dataset 1 and dataset 2. **C.** Correlation between z-transformed correlations by voxel for dataset 1 vs. dataset 2.

235 where in the brain, the inferences perform slightly better for regions with dense electrode sampling across
 236 patients. (Taken to the logical extreme, we could not hope to accurately recover activity patterns from
 237 brain areas where no recordings existed from any patient.) As more data are included in the inference
 238 procedure, this suggests that reconstruction accuracy should improve.

239 A fundamental assumption of the SuperEEG algorithm is that the data covariance matrix is stable
 240 over time and across people. This is a useful simplification. However, a growing body of evidence
 241 from the fMRI community suggests that the data covariance matrix changes in meaningful ways over
 242 time (for example, the data covariance matrix changes from moment-to-moment during story listening,
 243 serving as a unique “fingerprint” for each moment of the story; further, these task-driven timepoint-
 244 specific covariance fingerprints appear to be largely preserved across people [26, 27]). These findings
 245 indicate that the full-brain covariance matrix is not stable over time. Other recent work has shown that
 246 people’s resting state connectivity matrices may be used to uniquely identify individuals and predict
 247 fluid intelligence scores [25]. This indicates that the full-brain covariance matrix is not stable across
 248 people. If the fundamental stability assumptions that SuperEEG relies on are violated, how can the
 249 SuperEEG algorithm still accurately recover LFP data? It is important to recognize that the fact that

variability (over time or across people) is predictive (e.g. of cognitive states during story listening or fluid intelligence scores) does not necessarily mean that this variability is large in magnitude. Rather, we have long known that brain structure is tightly preserved across individuals (and over time, at least on the timescale of typical clinical and experimental recording sessions), and any functional changes must occur within the framework of the underlying structural anatomy. Nevertheless, one could imagine future improvements to the SuperEEG approach that leverage resting state fMRI or structural data [e.g. diffusion tensor imaging (DTI)] to estimate Bayesian priors over the correlation matrices inferred, in the current framing, using only ECoG data. Further, relaxing the assumption that the covariance matrix is stable (over time and/or across people), and/or incorporating more detailed brain conductance models (e.g. informed by structural MRI scans) may improve the predictive performance of the approach.

One potential limitation of the SuperEEG approach is that the above assumption of covariance stability across people may be violated even more if different patients are performing different cognitive tasks. To understand of the extent to which the current findings generalize across cognitive tasks, we replicated our initial findings using a dataset in which patients participated in two tasks, and limited the training data to either within task, across task, or using both tasks. Since we found the most accurate reconstructions using task-specific data, this would suggest building up new databases for estimating each task-specific covariance matrix. Or, using a more sophisticated approach, one could create a hierarchical model whereby each task-specific covariance matrix was modeled as a perturbation of a “global” task-unspecific covariance matrix (which could in turn be informed by fMRI or DTI data).

A second potential limitation of the SuperEEG approach is that it does not provide a natural means of estimating the precise timing of single-neuron action potentials. Prior work has shown that gamma band and broadband activity in the LFP may be used to estimate the firing rates of neurons that underly the population contributing to the LFP [28]. Because SuperEEG reconstructs LFPs throughout the brain, one could in principle use gamma or broadband power in the reconstructed signals to estimate the corresponding firing rates (though not the timings of individual action potentials).

275 Beyond providing a means of estimating ongoing activity throughout the brain using already im-
276 planted electrodes, our work also has implications for where to place the electrodes in the first place.
277 Electrodes are typically implanted to maximize coverage of suspected epileptogenic tissue. However,
278 our findings suggest that this approach could be further optimized. Specifically, one could leverage not
279 only the non-invasive recordings taken during an initial monitoring period (as is currently done), but also
280 recordings collected from other patients. We could then ask: given everything we know about the other
281 patients and from the scalp recordings of this new patient, where should we place a fixed number of
282 electrodes to maximize our ability to map seizure foci? As shown in Figure 5, recordings from different
283 locations are differently informative in terms of reconstructing the spatiotemporal patterns throughout
284 the brain. This property might be leveraged in decisions about where to surgically implant electrodes in
285 future patients.

286 **Concluding remarks**

287 Over the past several decades, neuroscientists have begun to leverage the strikingly profound mathemati-
288 cal structure underlying the brain’s complexity to infer how our brains carry out computations to support
289 our thoughts, actions, and physiological processes. Whereas traditional beamforming techniques rely on
290 geometric source-localization of signals measured at the scalp, here we propose an alternative approach
291 that leverages the rich correlational structure of a large dataset of human intracranial recordings. In do-
292 ing so, we are one step closer to observing, and perhaps someday understanding, the full spatiotemporal
293 structure of human neural activity.

294 **Code availability**

295 We have released an open-source SuperEEG Python toolbox. All of the code used in this manuscript is
296 on GitHub, and the code may be shared using a GitHub account accessible to the reviewers upon request.

297 **Data availability**

298 The dataset analyzed in this study was generously shared by Michael J. Kahana. A portion of the dataset
299 may be downloaded [here](#).

300 **Acknowledgements**

301 We are grateful for useful discussions with Luke J. Chang and Matthijs van der Meer. We are also grateful
302 to Michael J. Kahana for generously sharing the ECoG dataset we analyzed in our paper, which was
303 collected under NIMH grant MH55687 to MJK. Our work was also supported in part by NSF EPSCoR
304 Award Number 1632738. The content is solely the responsibility of the authors and does not necessarily
305 represent the official views of our supporting organizations.

306 **Author Contributions**

307 J.R.M conceived and initiated the project. L.L.W.O. and A.C.H. performed the analyses. J.R.M. and
308 L.L.W.O. wrote the manuscript.

309 **Author Information**

310 Reprints and permissions information is available at www.nature.com/reprints. The authors declare no
311 competing financial interests. Readers are welcome to comment on the online version of the paper.
312 Publisher's note: Springer Nature remains neutral with regard to jurisdictional claims in published maps
313 and institutional affiliations. Correspondence and requests for materials should be addressed to J.R.M.
314 (jeremy.r.manning@dartmouth.edu).

315 **References and Notes**

316 [1] R. J. Sawyer, *The Terminal Experiment* (HarperPrism, 1995).

317 [2] T. J. Sejnowski, P. S. Churchland, J. A. Movshon, *Nature Neuroscience* **17**, 1440 (2014).

- 318 [3] J. Sarvas, *Phys. Med. Biol.* **32**, 11 (1987).
- 319 [4] A. Z. Snyder, *Electroencephalography and Clinical Neurophysiology* **80**, 321 (1991).
- 320 [5] S. Baillet, J. C. Mosher, R. M. Leahy, *IEEE Signal Processing Magazine* **18**, 14 (2001).
- 321 [6] A. Hillebrand, K. D. Singh, I. E. Holliday, P. L. Furlong, G. R. Barnes, *Human Brain Mapping* **25**,
- 322 199 (2005).
- 323 [7] R. J. Huster, S. Debener, T. Eichele, C. S. Herrmann, *The Journal of Neuroscience* **32**, 6053 (2012).
- 324 [8] C. E. Rasmussen, *Gaussian processes for machine learning* (MIT Press, 2006).
- 325 [9] P. B. Sederberg, M. J. Kahana, M. W. Howard, E. J. Donner, J. R. Madsen, *Journal of Neuroscience*
- 326 **23**, 10809 (2003).
- 327 [10] P. B. Sederberg, *et al.*, *Cerebral Cortex* **17**, 1190 (2007).
- 328 [11] P. B. Sederberg, *et al.*, *Psychological Science* **18**, 927 (2007).
- 329 [12] J. R. Manning, S. M. Polyn, G. Baltuch, B. Litt, M. J. Kahana, *Proceedings of the National Academy*
- 330 *of Sciences, USA* **108**, 12893 (2011).
- 331 [13] J. R. Manning, M. R. Sperling, A. Sharan, E. A. Rosenberg, M. J. Kahana, *The Journal of Neuro-*
- 332 *science* **32**, 8871 (2012).
- 333 [14] Y. Ezzyat, *et al.*, *Current Biology* **27**, 1 (2017).
- 334 [15] P. C. Horak, *et al.*, *Epilepsia* **58**, 373 (2017).
- 335 [16] J. E. Kragel, *et al.*, *NeuroImage* **155**, 70 (2017).
- 336 [17] M. T. Kucewicz, *et al.*, *Brain* **140**, 1337 (2017).
- 337 [18] J.-J. Lin, *et al.*, *Hippocampus* **27**, 1040 (2017).

- ³³⁸ [19] E. A. Solomon, *et al.*, *Nature Communications* **In press** (2018).
- ³³⁹ [20] C. T. Weidemann, *et al.*, *Journal of Experimental Psychology: General* **In press** (2018).
- ³⁴⁰ [21] Y. Ezzyat, *et al.*, *Nature Communications* **9**, <https://www.doi.org/10.1038/s41467> (2018).
- ³⁴¹ [22] M. T. Kucewicz, *et al.*, *Brain* **141**, 971 (2018).
- ³⁴² [23] J. R. Manning, R. Ranganath, K. A. Norman, D. M. Blei, *PLoS One* **9**, e94914 (2014).
- ³⁴³ [24] B. T. T. Yeo, *et al.*, *Journal of Neurophysiology* **106**, 1125 (2011).
- ³⁴⁴ [25] E. S. Finn, *et al.*, *Nature Neuroscience* **18**, 1664 (2015).
- ³⁴⁵ [26] E. Simony, C. J. Honey, J. Chen, U. Hasson, *Nature Communications* **7**, 1 (2016).
- ³⁴⁶ [27] J. R. Manning, *et al.*, *bioRxiv* p. 106690 (2017).
- ³⁴⁷ [28] J. R. Manning, J. Jacobs, I. Fried, M. J. Kahana, *The Journal of Neuroscience* **29**, 13613 (2009).